Part 4. Effects of pre-existing space charge on positive discharge development

Les Renardières Group

Indexing terms: *Arcing, Breakdown and gas discharges, Gas discharges, Load and voltage regulation, Overvoltages*

Abstract: The paper describes one of the three major studies with double impulses performed during the fifth test period of the Les Renardières Group. In the third experiment a negative impulse (T_{cr} = 45 μs) was used to create an extensive space charge in a 6 m rod-rod gap. The voltage level selected was $\sim 0.8 U_{50-}$. Thereafter the effect of this pre-existing space charge on the development of a subsequent positive discharge was investigated. The positive discharge was initiated by applying a positive impulse (240/2500 μs) to the previously unenergised electrode at the associated U_{50+} level. The spatial and temporal characteristics of the pre-existing space charge were varied over a wide range, first, by utilising wavetail values of either 180 or 9000 μs, and, secondly, by selecting the time delay Δt to the application of the positive impulse such that Δt lay in the range $0 \leqslant \Delta t \leqslant$ 300 ms. The evolution of the pre-existing space charge is seen to be strongly dependent on the time-to-half value $T_{1/2}$ of the negative impulse, and, for $T_{1/2}$ = 180 μs, the phenomenon of reverse discharges is observed in the region of the gap adjacent to the negative electrode. Development of the positive discharge is observed to be associated with a leader propagation phase which clearly interacts with the pre-existing space charge, such that the characteristic properties of the leaders (velocity, current) remain essentially constant throughout the test range. The breakdown data (U_{50+}) indicate that large reductions in withstand ($\sim$50%) are achieved with the short $\Delta t/T_{1/2}$ values, and that recovery of the gap to an effective space-charge-free condition requires $\Delta t \simeq 100 T_{1/2}$.

1 Introduction

As discussed in Part 1, the breakdown of phase-to-phase insulation is influenced by the manner in which the voltage between the phases is subdivided into its positive and negative components. In most practical cases, the resultant discharge is governed mainly by the phenomena associated with the positive electrode. When the negative impulse precedes the positive one, the negative impulse can create sufficient discharge activity in the gap such as to leave a bulk space charge which, following energisation of the second electrode, can interact with the subsequent positive discharge. It has been established that, owing to such pre-existing space charges, significant reductions in gap withstand capability can occur over periods of several milliseconds [1–4]. However the physical aspects which lead to and sustain such reductions have not been examined in detail. Consequently, the main aim of this series of experiments was to investigate the interaction of such a pre-existing space charge with the development of a positive discharge.

2 Test configuration and test procedure

In the present study a 6 m rod-rod gap located 16.7 m above the laboratory floor was used, see Part 1. Different terminations were fitted to the 100 mm rods, namely, a hemisphere of 50 mm radius and a sphere of 125 mm radius. These terminations ensured that on the application of a negative voltage to the hemispherically ended rod no discharge developed at the positive electrode, even for the highest negative voltage level employed. This freedom from premature positive discharge was maintained despite the enhancement of the Laplacian field at the anode surface by the space charge field of the negative discharge. The discharge at the negative electrode constitutes the source of the pre-existing space charge. Following the application of the negative impulse to the hemispherically ended rod, a positive impulse was applied to the spherically ended rod after a time delay Δt (see Fig. 1) and the development of the positive discharge was initiated.

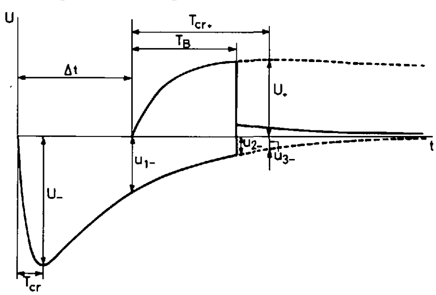

Fig. 1 *The time sequence of the negative and positive voltage impulses and related parameters*

u_{2-} is the negative voltage component at breakdown

The time sequence of the negative and positive voltage impulses and related parameters are shown in Fig. 1. For the negative impulse a constant time to crest T_{cr} of 45 μs was employed with either a short or a long wavetail, namely, a value of $T_{1/2}$ of 180 μs or 9000 μs. Owing to the chopping of the impulse generator polytron gaps [5], the effective total duration of the 9000 μs wavetail was $\simeq$32 000 μs. The purpose of varying the negative wavetail was to influence the spatial behaviour of the newly created space charge prior to the application of the positive impulse. The waveshape of the positive impulse was held constant throughout the investigation at 240/2500 μs. This approximately critical waveshape was chosen to ensure breakdown in the proximity of the crest value.

Initially the characteristics of the space charge, created by the negative impulse acting alone, were investigated at several values of U_-. Thereafter, a constant value of U_- was employed for the majority of the investigation, namely

Paper 4828A (S3) received 14th January 1986
For author details see Paper 4825A, Double-impulse tests of long airgaps Part 1

$U_- = -2250$ kV. A few tests were conducted using $U_- = -1800$ kV. It should be noted that, for the negative impulse alone, the 50% breakdown voltage U_{50-} was approximately 2750 kV.

For $U_- = -2250$ kV and various values of Δt, the magnitude of the positive impulse voltage was selected to enable the determination of U_{50+} using the up-and-down method. As a reference, the U_{50+} was also determined for a space-charge-free gap, i.e. $\Delta t = \infty$.

To quantify the space charge created by the negative impulse, measurements were made of the apparent charge flow at the hemispherical-rod electrode and of the electric field at the spherical-rod electrode, see Part 1. The spatial and temporal development of the discharge were recorded using both image convertor and still cameras, with particular attention being paid to the positive discharge. The measurement of the electric field at the sphere was supplemented with a measurement of the discharge current. With respect to the charge measurements, the term apparent charge is appropriate, as the measured charge q_m is not necessarily a direct measure of the charge q created in the gap.

The electric field of the gap was determined using the charge simulation method [6]. The axial electric field strength $E_g(z)$ is shown in Fig. 3 of Part 1. The asymmetry of the geometric electric field implies that, for finite values of $u_-(t)$ and $u_+(t - \Delta t)$, a simple numerical summation of these voltages is unrepresentative of the electrical stress in the gap. For example, the axial stress at the electrodes is given by

$$\frac{E_g(0)}{\text{kV mm}^{-1}} = 5.36\frac{u_+(t - \Delta t)}{\text{MV}} - 0.89\frac{u_-(t)}{\text{MV}} \tag{1}$$

and

$$\frac{E_g(d)}{\text{kV mm}^{-1}} = 1.76\frac{u_+(t - \Delta t)}{\text{MV}} - 10.9\frac{u_-(t)}{\text{MV}} \tag{2}$$

The origin of the axial co-ordinate z is taken to be at the tip of the spherical-rod electrode ($z = 0$) and hence the tip of the hemispherical-rod electrode is associated with $z = d$, d being the gap length.

3 Breakdown voltages and time lags

The breakdown voltage parameters are listed in Table 1, together with the mean time to breakdown $\bar{T}_B$ associated with each up-and-down sequence; i.e. this value represents the mean of all values of T_B recorded at the different voltage levels of the up-and-down sequence. As an indication of the range of T_B encountered, column 9 of Table 1 also lists the minimum and maximum values recorded at each Δt.

From $\bar{T}_B$ and the minimum values of T_B it is clear that in several of the U_{50+} determinations the breakdown did not occur exactly at the crest of the impulse. However, following standard practice, the positive breakdown voltage was always equated to the prospective peak value. In addition, reference is made to particular u_- values attained during the application of the positive impulse, namely u_{1-}, u_{2-} and u_{3-}, see Fig. 1. No corrections for atmospheric conditions have been made to the U_{50+} values, as the ambient conditions were essentially constant during the test period (an atmospheric pressure $\simeq 0.1015$ MPa at $\simeq 19$°C with a humidity of $\simeq 6$ g/m^3).

The breakdown voltages were also determined for syn-

Table 1 : Breakdown parameters for the different test conditions

$T_{1/2}$ µs	U_- kV	Δt µs	u_{1-} kV	u_{2-} kV	u_{3-} kV	U_{50+} kV	$\sigma(U_{50+})$ kV	$\bar{T}_B$ µs	$\sigma(\bar{T}_B)$ µs
—	—	∞	—	—	—	2080	156	248 (180–515)	74
-180	-1800	500	-120	-30	-30	1785	175	235 (189–316)	41
		1000	0	0	0	1855	135	234 (189–316)	36
		2000	0	0	0	1840	115	223 (174–298)	32
	-2250	200	-980	-260	-215	1340	119	214 (135–270)	37
		500	-150	-40	-40	1470	105	213 (159–255)	34
		1000	0	0	0	1575	255	221 (170–301)	32
		1500	0	0	0	1570	79	218 (115–318)	50
		2000	0	0	0	1595	94	237 (197–292)	26
		10000	0	0	0	~1790	—	225 (210–234)	12
9000	-2250	10000	-1050	-1045	-1035	870	145	202 (174–244)	19
		30000	-200	-195	-190	1225	39	288 (244–394)	34
		40000	0	0	0	1480	86	296 (225–408)	41
		100000	0	0	0	1600	175	282 (247–361)	30
		300000	0	0	0	1845	177	251 (213–368)	42
180	-2250	0	0	-1880	-775	805	43	94.5 (57–149)	3
9000	-1235	0	0	-1225	-1220	1220	118	192 (150–294)	27

chronously applied impulses, i.e. $\Delta t = 0$, and these are given in Table 1 for comparison. Although the synchronism strictly applies only with respect to the origins of the two impulses, there was also, in the case of the 9000 μs negative impulse, effective synchronism of crest voltage.

For a constant U_-, the variation of U_{50+} and of the total breakdown voltage $(U_{50+} - u_{2-})$ with u_{2-} are shown in Fig. 2. The reduction in U_{50+}, curve A, indicates

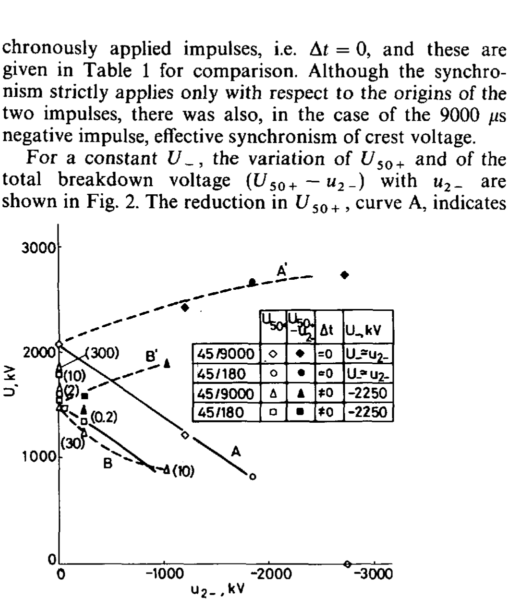

Fig. 2 *Dependence of U_{50+}, curves A and B, and total voltage $(U_{50+} - u_{2-})$, curves A' and B', on the negative voltage component at breakdown, u_{2-}*

For some selected shots the associated time delay between impulses (Δt) is indicated within brackets. The units are in milliseconds

the important influence of the u_{2-} component on breakdown when applying synchronous impulses. It is seen that, with an increasing u_{2-} component, the necessary U_{50+} is decreased, although as depicted by curve A' an increase is observed in the total breakdown voltage. In addition a comparison with the breakdown voltages obtained with nonsynchronous impulses (curve B, $u_{2-} < 0.5U_-$) shows that a maximum reduction in U_{50+} occurs in the range $1 < \Delta t/T_{1/2} < 10$. This observed reduction is in agreement with previous work, e.g. see Reference 7. To a first approximation, curve B can be assumed to be linear. Curve B' represents the total breakdown voltage under these latter conditions.

The variation of $U_{50+}(\Delta t)/U_{50+}(\infty)$ is shown in Fig. 3, from which it is clear that the effect of the pre-existing space charge is to produce a reduction in U_{50+}. The greater reduction obtained with $U_- = -2250$ kV, compared with $U_- = -1800$ kV, indicates that, because the magnitude of U_- controls the amount of space charge in the gap, the greater reduction is associated with an increased space charge. In Fig. 3, it should be noted that,

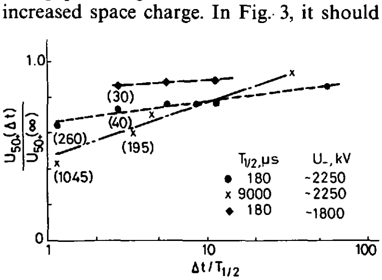

Fig. 3 *Positive U_{50+} values for various Δt as a function of $\Delta t/T_{1/2}$*

$U_{50+}(\Delta t)$ is normalised to the positive U_{50} obtained for a space-charge-free condition, i.e. $\Delta t = \infty$. The values enclosed in brackets denote the magnitude of the negative voltage component at breakdown u_{2-}, kV.

for particular Δt values, there exists a measureable negative voltage u_{2-} at the instant of breakdown. In addition, the measurements indicate that the duration of the negative impulse ($T_{1/2}$) has a major effect on the U_{50+} values. Initially the 9000 μs wavetail is associated with a greater reduction in U_{50+} than that observed with the 180 μs wavetail. Thereafter, for increasing values of $\Delta t/T_{1/2}$, the percentage reductions decrease. For $\Delta t/T_{1/2} > 10$ however, the greater reduction becomes associated with the shorter tail, namely 180 μs, for which reductions of between 5%–15% are recorded. Finally, from Fig. 3, it may be concluded that, for real times approaching $100T_{1/2}$, conditions in the interelectrode space approach those associated with the space-charge-free gap.

4 Space charge created by the negative impulse

4.1 Charge measured up to $T_{cr} = 45$ µs

Although a detailed investigation of the negative discharge development was outside the aim of the present study, the experimental evidence from the image convertor records suggests that the phenomena involved are basically the same as those observed previously in rod-plane gaps [8]. The image-convertor picture and related charge oscillogram (see Fig. 4) show the temporal evolution leading to

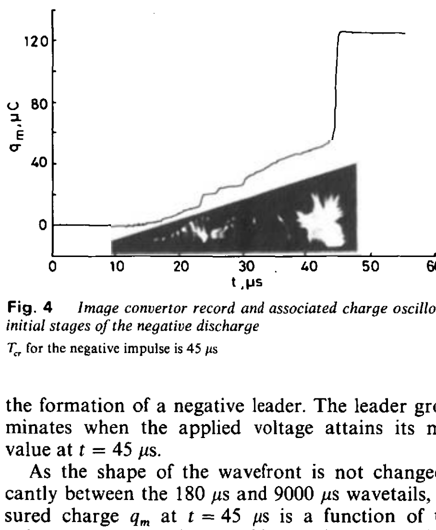

Fig. 4 *Image convertor record and associated charge oscillogram of the initial stages of the negative discharge*

T_{cr} for the negative impulse is 45 μs

the formation of a negative leader. The leader growth terminates when the applied voltage attains its maximum value at $t = 45$ μs.

As the shape of the wavefront is not changed significantly between the 180 μs and 9000 μs wavetails, the measured charge q_m at $t = 45$ μs is a function of the peak voltage only. In Fig. 5*a* this relationship is illustrated together with a histogram of these q_m values at -2250 kV. A ratio of about 4 : 1 can exist between the maximum and minimum values.

The spatial extent of the negative discharge, as deduced from the image convertor records, is in turn related to the measured charge. Fig. 5*b* indicates that a linear relationship exists between q_m and the axial discharge length z_L. This relationship is of the order 50 $\mu C/m$.

From the above data a negative voltage level of -2250 kV was selected because, at this voltage level, the positive electrode (spherical-rod) remained discharge-free, while still permitting a large space charge to be created in both magnitude and spatial extent from the negative (hemispherical-rod) electrode.

4.2 Space charge behaviour for $T_{1/2} = 180$ µs

Following the termination of the negative discharge growth at $t = 45$ μs, it was observed that the measured charge decreased significantly during the impulse tail. The decrease was associated with discharge processes because

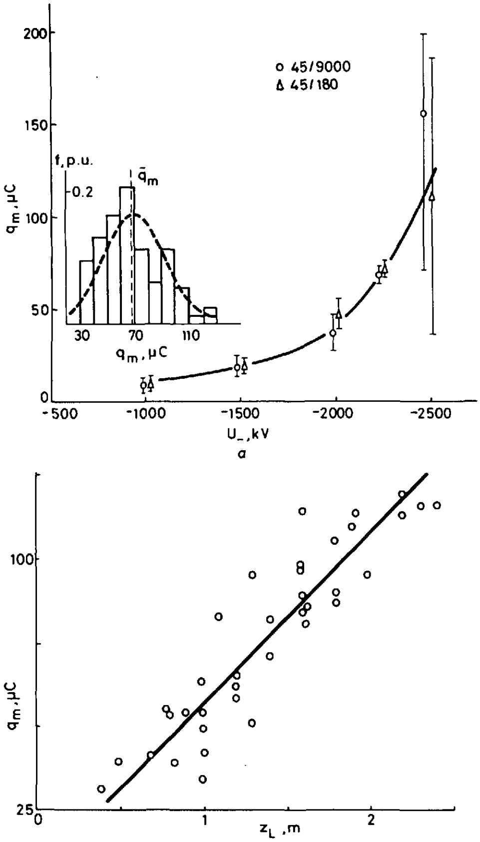

Fig. 5 (*a*) *The measured charge q_m as a function of the peak value of the negative impulse U_- and* (*b*) *q_m as a function of the axial length of the negative discharge z_L*

a A histogram (insert) illustrates the scatter in q_m encountered with $U_- = -2250$ kV

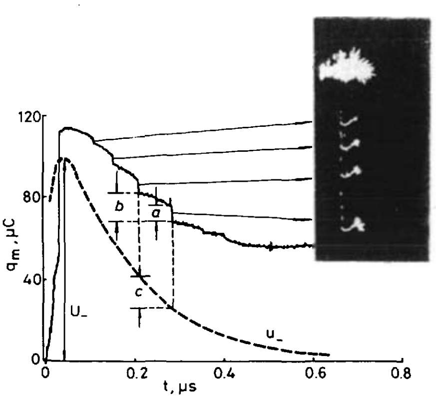

Fig. 6 *Image convertor record and charge oscillogram obtained for the 180 μs wavetail*

The decay of the negative impulse voltage is included. $a \equiv q_{ms}$, $b \equiv q_{md}$ and $c \equiv \Delta u_-$.

only a negligible correction to the charge records arose from the capacitive component. Fig. 6 shows a typical pattern of the charge signal together with the relevant image convertor picture. The signal exhibits step-like decays q_{ms} which can be associated with reilluminations of the leader channel. Between steps the charge signal decreases continuously, and, during such a phase, an intermittent, weakly luminous phenomenon can be observed near the rod tip.

Reilluminations of the leader channel could result from a reversal of the electric field in the region of the cathode (rod electrode), and in conjunction with the q_m records these observations suggest that a reverse discharge has occurred. Necessary conditions are that the applied negative voltage attains a sufficiently low amplitude, and that a net negative-space-charge cloud exists in the gap. Similar observations have been reported in which the observed optical phenomena (reilluminations/luminous glow) clearly encompassed positive discharge characteristics [9].

Fig. 7 shows that the times at which the leader reilluminations occur are exponentially related such that the decrease in the applied voltage between consecutive reilluminations Δu_- attains an approximately constant value.

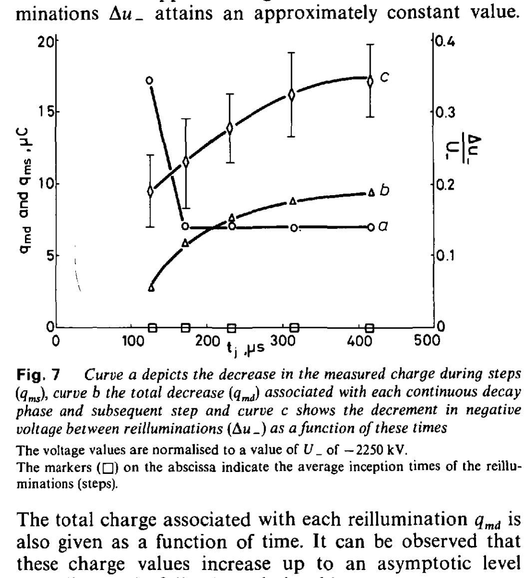

Fig. 7 *Curve a depicts the decrease in the measured charge during steps (q_{ms}), curve b the total decrease (q_{md}) associated with each continuous decay phase and subsequent step and curve c shows the decrement in negative voltage between reilluminations (Δu_-) as a function of these times*

The voltage values are normalised to a value of U_- of -2250 kV.

The markers (□) on the abscissa indicate the average inception times of the reilluminations (steps).

The total charge associated with each reillumination q_{md} is also given as a function of time. It can be observed that these charge values increase up to an asymptotic level according to the following relationship

$$q_{md}(t_j) = K[1 - e^{-t_j/\tau}] \qquad (3)$$

where t_j is the time to the jth reillumination. It is of interest to note that the derived time constant τ (= 185 μs) is similar to that for the applied voltage decay, namely 160 μs. Following this reillumination phenomenon, the remanent space-charge level (q_{mr}) at $t \sim \Delta t$ is shown as a normalised quantity in Fig. 8.

4.3 Space-charge behaviour for $T_{1/2} = 9000$ μs

As practically the same wavefront is utilised, the initial negative discharge phenomenon remains unchanged. However, owing to the very long wavetail (9000 μs), the evolution of the space charge during the voltage decay differs in several respects from that observed with the 180 μs tail. For $t > 45$ μs, the charge oscillogram (Fig. 9) exhibits an increasing value up to $t \sim 5000$ μs. Thereafter a slow decay is observed which appears to have several time constants. A definite change in slope can be observed at

18 000 μs, while at 32 000 μs the sudden variation coincides with the inherent discontinuity in the applied voltage, see

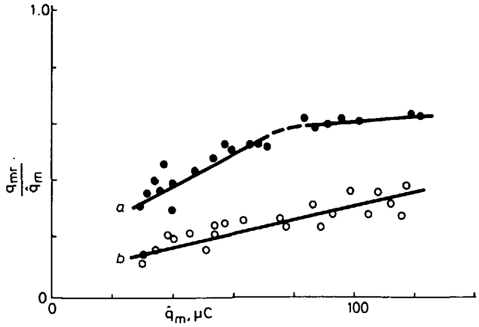

Fig. 8 *The remanent space charge q_{mr} following the 9000 μs tail (curve a, t = 95 000 μs) and the 180 μs tail (curve b, t = 5000 μs) normalised to $\hat{q}_m$, the relevant maximum value*

$T_{1/2}$ = 180 μs, $\hat{q}_m$ is at $t \sim 45$ μs
$T_{1/2}$ = 9000 μs, $\hat{q}_m$ is at $t \sim 5000$ μs

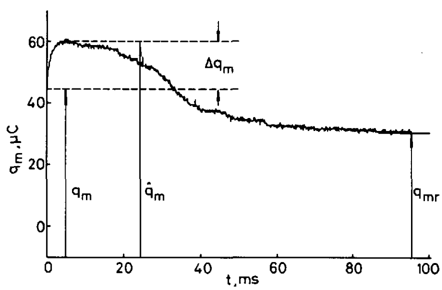

Fig. 9 *Charge evolution associated with the 9000 μs wavetail*

Δq_m is the maximum increase in charge above the value q_m measured at $t = 45$ μs. The remanent charge prior to time Δt is denoted by q_{mr}.

Section 2. It should be noted, however, that the rapid decrease in the recorded charge at this time is much larger than that associated with the purely capacitive response of the measuring section. Reilluminations are not detected on the wavetail.

Contrary to the situation with the 180 μs wavetail, there is clear indication that, after the negative discharge has ceased to grow, charge drift occurs for $t > 45$ μs. This ionic drift is brought about by the action of the geometric electric field, which, for $T_{1/2} = 9000$ μs, remains significant for several milliseconds. An analysis of the charge oscillograms indicates that the increase in the measured charge due to drift Δq_m is inversely related to the q_m value at $t = 45$ μs, see Figs. 9 & 10. As already observed, a larger q_m value implies a greater axial extent to the negative discharge. These observations thus suggest that, for increased q_m, the ions involved in this drift are located at points progressively removed from the negative electrode.

The subsequent decrease in the charge oscillograms suggest that ion losses become effective for $t > 5000$ μs. Possible mechanisms to account for these observations are recombination and diffusion. There is no particular evidence of reverse discharges due to possible field reversal, but the change in slope at 18 000 μs could be indicative of negative-ion impingement on the negative electrode. An observation of this nature has been reported in short gap studies [10].

The remanent charge as a function of the maximum charge $\hat{q}_m$ is shown in Fig. 8, together with the short-tail data. It can be seen that a larger remanent space charge exists even after the much longer time intervals associated

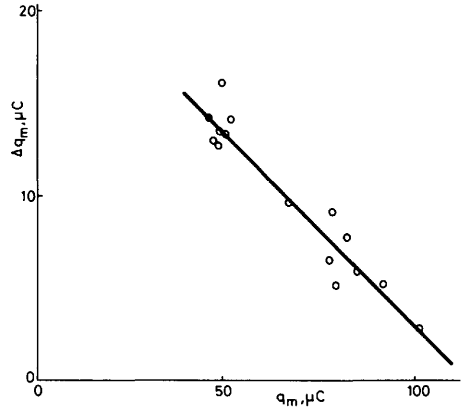

Fig. 10 *The incremental change in measured charge Δq_m as a function of q_m, the associated value recorded at t = 45 μs*

with the 9000 μs wavetail. The duration of this space charge indicates that an influence on the subsequent positive discharge can still be expected following the long Δt values.

5 Positive discharge development in the presence of a pre-existing space charge

5.1 General characteristics

Typical spatiotemporal image-convertor records of the positive leader development and breakdown phase are shown in Fig. 11. A schematic diagram is included which underlines the main features of the positive-discharge development, and, in addition, indicates the time relationship with the pre-existing space charge created by the negative impulse. The approximate axial extent of the negative discharge is also depicted.

The basic data obtained from an analysis of these IC records are presented in Table 2, together with the parameters associated with the relevant impulse voltages. A breakdown voltage reference level is provided from the test conducted with a positive impulse alone.

The IC records display an interesting feature during the later stages of the positive-leader-corona development. It is observed that a rapid axial elongation of this phase can occur in the presence of the pre-existing space charge. However, the more important aspect is that, without the presence of this space charge, no pronounced leader phenomenon would occur, especially at the lowest voltage levels, see Table 2. In addition, the leader propagation (mean axial velocity) is apparently little affected. A further point of interest is the respective leader lengths at the instant of breakdown. An axial propagation is seen to occur under the 9000 μs tail, which exceeds even that for the positive impulse alone (see Fig. 11*b*), even although the voltage across the gap is up to 40% lower.

As the leader growth is the longest event in both spatial extent and time, the important engineering parameters of time to breakdown $\bar{T}_B$ and the associated standard deviation $\sigma(\bar{T}_B)$ directly reflect this stage of the breakdown process. Consequently, the small variation observed in the leader velocities suggest that, in each case, the pre-existing charge must compensate the reduced geometric field in such a manner that conditions for leader propagation become identical. A study of the space-charge field and its influence in the region of the positive electrode is therefore essential before a detailed investigation of the leader and leader-corona stage is undertaken.

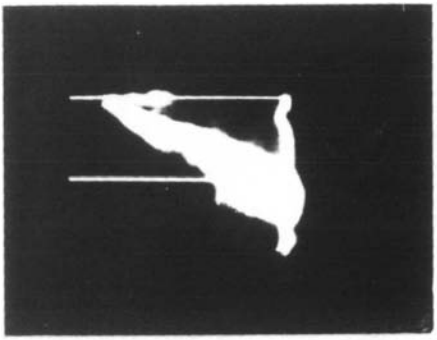

a

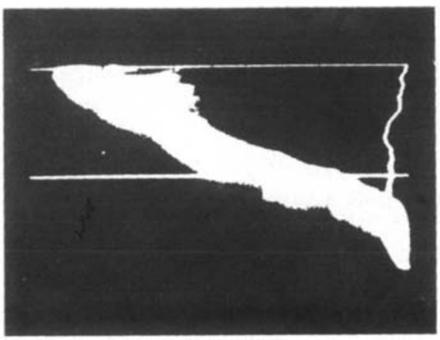

b

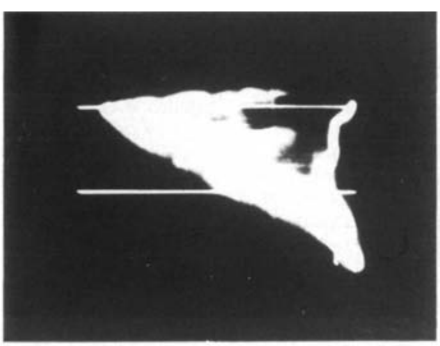

c

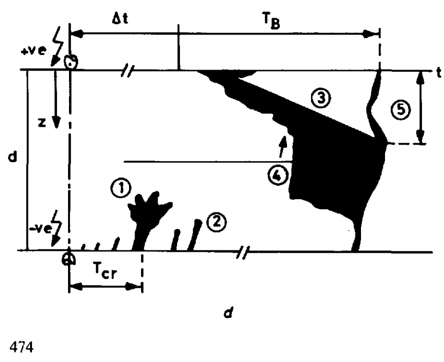

d

Fig. 11 *Typical image convertor records of the positive discharge phenomenon*

The schematic diagram indicates the major phases of the discharge and the approximate spatiotemporal relationships with respect to the negative phenomenon.
(*a*) $T_{1/2}$ = 180 μs, Δt = 1500 μs, T_B = 182 μs
(*b*) $T_{1/2}$ = 9000 μs, Δt = 300 000 μs, T_B = 311 μs
(*c*) Positive impulse only, $\Delta t = \infty$, T_B = 223 μs
(*d*) 1 Negative impulse corona
2 Reilluminations of the negative corona
3 Positive leader
4 Positive leader corona, showing elongation
5 Length of positive leader at instant of breakdown.

Table 2: Basic discharge parameters

$T_{1/2}$ μs	U_- kV	Δt μs	U_{50+} kV	$\bar{T}_B$ μs	$\bar{v}_z$ mm/μs	$\bar{L}_t$ m	$\bar{I}$ A
—	—	∞	2080	248	14.7	2.8	1.5
180	−1800	500	1785	235	13.8	2.4	1.2
		1000	1855	234	14.4	2.4	1.2
		2000	1840	223	14.5	2.4	—
	−2250	200	1340	214	14.7	2.8	—
		500	1470	213	14.0	2.4	0.85
		1000	1575	221	13.8	2.5	0.9
		1500	1570	218	14.7	2.5	1.0
		2000	1595	237	13.8	2.7	0.95
		10000	∼1790	225	14.0	2.7	1.25
9000	−2250	10000	870	202	14.3	2.4	0.8
		30000	1225	288	14.4	3.5	0.9
		40000	1480	296	14.7	3.6	0.95
		100000	1600	282	14.8	3.4	1.1
		300000	1845	251	15.6	3.2	—

$\bar{v}_z$ = average axial velocity of positive leader
$\bar{L}_t$ = average axial extent of the positive leader at the instant of breakdown
$\bar{I}$ = mean current during the continuous propagation of the positive leader

5.2 *Influence of the pre-existing space charge at t = Δt*

The electrostatic field at the positive electrode was monitored with a capacitive probe. Oscillographic recordings confirmed that this electrode surface remained discharge-free for $t \leqslant \Delta t$, after which the positive impulse voltage was applied. It is therefore possible to obtain accurate values of the space-charge field within this time range. A typical oscillographic record is shown in Fig. 12, in which the relevant parameters are indicated. The polarity of the recorded signal indicates that, at the positive electrode, the remanent space charge appears as a net negative charge configuration. On subtraction of the applied electrostatic

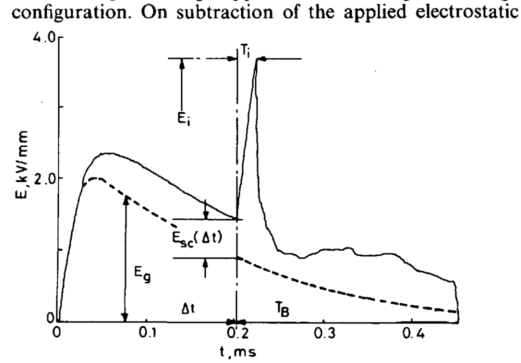

Fig. 12 *The electrostatic field variations recorded at the positive electrode as a function of time*

The relevant parameters shown are:
Δt = delay time to positive impulse application
E_g = geometric field component of the negative impulse
$E_{sc}(\Delta t)$ = space charge field component at time Δt
E_i = positive corona inception field strength
T_i = time to positive corona inception, Δt is time zero
T_B = time to breakdown, Δt is time zero.

field component, these time-resolved records (Fig. 12) allow details in the evolution of the space-charge field to be observed. Records of this nature are presented in Fig. 13 and include the associated charge development.

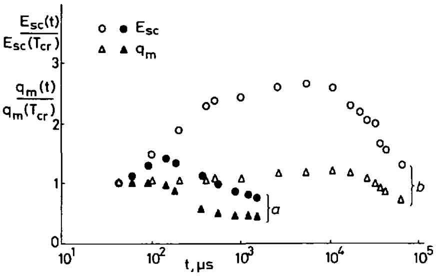

Fig. 13 *Evolution of the pre-existing space charge $q_m(t)$ and its associated field $E_{sc}(t)$ at the positive electrode boundary*

The charge measuring device is located in the negative electrode:
(*a*) $T_{1/2} = 180$ μs; (*b*) $T_{1/2} = 9000$ μs

To account for these time-dependent observations a redistribution of the space charge within the gap volume must occur. Under the 9000 μs wavetail a pertinent process is ionic drift, and, for long Δt, mutual repulsion of the space charge cloud should be considered. For the 180 μs wavetail, the redistribution of the space charge should be examined on the basis of the potential recovery of the negative electrode.

Fig. 14 shows, for the specific values of Δt employed, the

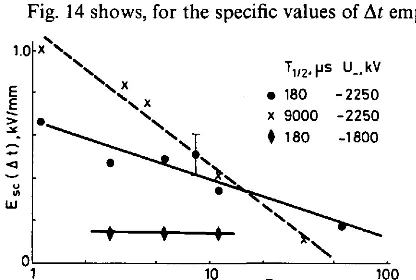

Fig. 14 *Space charge field strength $E_{sc}(\Delta t)$ as a function of the parameter $\Delta t/T_{1/2}$*

space-charge field E_{sc} as a function of $\Delta t/T_{1/2}$. The values of E_{sc} are those pertaining at the instant of the positive voltage application ($t = \Delta t$). A comparison with the breakdown data of Fig. 3 is of interest because the crossover point at $\Delta t \approx 10T_{1/2}$ is similarly in evidence. This suggests that the U_{50+} values are directly compensated by the space-charge field such that, irrespective of the applied voltage level, the leader phenomena become essentially identical. For short Δt values, the presence of the negative voltage component should be considered, see Section 2.

Owing to the large scatter in the amount of negative space charge created at a constant voltage level (Fig. 5*a*), it can be of interest to study the influence of such a scatter on the probability of breakdown for the case of the positive voltage applied at the U_{50+} level. Fig. 15*a* indicates that there is a correlation between the amount of negative charge created and the frequency of breakdown, irrespective of the particular U_{50+} level studied. The distribution of breakdowns as a function of the amount of negative charge (see Fig. 15*b*) is obtained by accumulating the results associated with the different U_{50+} values. From this analysis, it is obvious that, at any U_{50+} level, the statistical feature of the breakdowns is not only due to the randomness of the positive discharge, but is strongly influenced by the statistical nature of the pre-existing negative space charge.

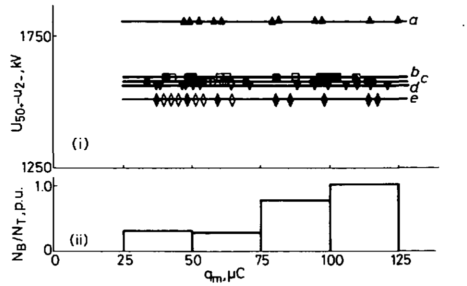

Fig. 15 (*i*) *Breakdown patterns at various total voltage levels ($U_{50+} - u_{2-}$) and* (*b*) *relative breakdown frequency*

The filled markers represent breakdown, the open withstands.
(*a*) $\Delta t = 10000$ μs; (*b*) $\Delta t = 2000$ μs; (*c*) $\Delta t = 1000$ μs; (*d*) $\Delta t = 1500$ μs and (*e*) $\Delta t = 5000$ μs

5.3 Analysis of the positive corona inception

The basic discharge data pertinent to the onset of the positive corona are summarised in Table 3, where $\bar{E}_i$ is the average inception field strength at the positive electrode. $\bar{T}_i$ is the associated time to inception as measured from the instant of application of the positive impulse (240/2500 μs). In Table 3, $T_{1/2}$ refers to the wavetail of the negative impulse, and $\hat{E}_{sc}$ is the maximum value of the associated space-charge fields, i.e. when $\Delta t = 1.11T_{1/2}$.

It is seen that the inception times, irrespective of the magnitudes of the pre-existing space charge, do not differ significantly from that observed with the positive impulse alone. However, the field strength at inception is considerably influenced by the presence of the space charge and falls to approximately 85% of the positive-impulse value of 4.1 kV/mm. Normalised inception data ($E_i(\Delta t)/E_i(\infty)$) are given in Table 4 for the various values of $\Delta t/T_{1/2}$ at constant U_- ($= -2250$ kV), where Δt is the time delay to the positive impulse. $E_i(\infty)$ is used to denote the condition of zero pre-existing charge. From these tabulated results, it is seen that the greater the space charge the lower the inception field strength, and that these reductions are approx-

Table 3: Corona inception data ($U_- = -2250$ kV)

$T_{1/2}$ μs	$\bar{E}_i$ kV/mm	$\bar{T}_i$ μs	$\hat{E}_{sc}$ kV/mm
180	3.65 ± 0.1	23.3 ± 0.8	≲0.60
9000	3.50 ± 0.2	22.5 ± 1.0	≲1.00
— (only U_+)	4.10 ± 0.2	23.3 ± 2.0	—

Table 4: Normalised corona inception data ($U_- = -2250$ kV)

$T_{1/2}$ μs	$\Delta t/T_{1/2}$	$\frac{E_i(\Delta t)}{E_i(\infty)}$
180	1.11	0.94
	2.78	0.88
	5.56	0.88
	8.33	0.88
	11.11	0.85
	55.56	0.88
9000	1.11	0.85
	3.33	0.82
	4.44	0.85
	11.11	0.83
	33.33	0.91

imately constant for $\Delta t/T_{1/2}$ in the range $2 < \Delta t/T_{1/2} < 12$. [A reduction in U_- of 20% raises the ratio of $E_i(\Delta t)/E_i(\infty)$ to an average of 0.92, which reflects the reduced value of the space charge, see Fig. 5*a*].

The role of the pre-existing space charge at corona inception may be elucidated by considering the following aspects:

(i) the corona inception times

(ii) the augmentation of the electrostatic field by the space-charge field E_{sc} as illustrated through Fig. 16.

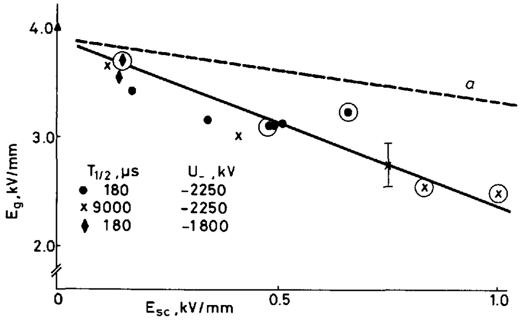

Fig. 16 *The total geometric field strength E_g at the positive electrode at the instant of corona inception T_i as a function of the space-charge field E_{sc}*

The open circles indicate the presence of a negative voltage component. The dotted curve (a) is the total field, $E_g + E_{sc}$.

The theoretical corona inception field for the positive sphere will be $\simeq 3.3$ kV/mm, and, consequently, all the inception levels reflect an overvoltage condition. As T_i is unchanged, the space-charge field apparently reduces the statistical time lags and thus acts as a sweep field. However, a certain minimum time appears to be necessary because under the short-tailed impulse $E_i(\Delta t)$ increases significantly for $\Delta t \lesssim 2T_{1/2}$.

The data of Fig. 16 show that, when the space-charge field is present, corona inception becomes possible with a reduced geometric field. The total field values are, however, such that $E_i(\Delta t) < E_i(\infty)$. Because, at these lower inception fields, the growth of the corona is maintained and the leader eventually launched, it is apparently the total field distribution which is of major importance. At corona inception, the space-charge field at the positive electrode is <20% of the instantaneous geometric field. However, the space-charge field will fall less rapidly with distance from the positive electrode than the applied field, which decreases to $\simeq 1\%$ of its maximum value at a distance of only 1 m from the electrode boundary.

5.4 Leader inception, propagation and breakdown

Values of the (total) geometric field strengths corresponding to the inception times of the positive leaders are illustrated in Fig. 17. Values are referred to the inception field strength for the positive impulse alone. Included in this Figure are data of the respective space-charge fields. It is clear that, although of relatively small value, the space-charge fields considerably influence the inception of the leader phase. For short Δt values there exists a negative voltage component, the influence of which cannot be readily identified.

A further observation is that, irrespective of the initial conditions, the leader velocities are almost identical, see Table 2. Because, at the instant of breakdown, the geometric field magnitudes for the various Δt values differ by up to 100%, the compensating role of the pre-existing space-charge field is again in evidence.

A typical composite record of the leader and breakdown phase of the discharge is shown in Fig. 18. The

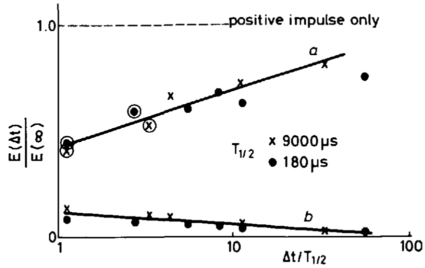

Fig. 17 *Curve (a) illustrates the total geometric field strength at positive leader inception as a function of $\Delta t/T_{1/2}$ and curve (b) indicates the associated space-charge fields*

The points enclosed by circles indicate the presence of a negative voltage component.

All values are referred to the leader inception field strength under the positive impulse alone; namely $E(\infty) = 7.98$ kV/mm

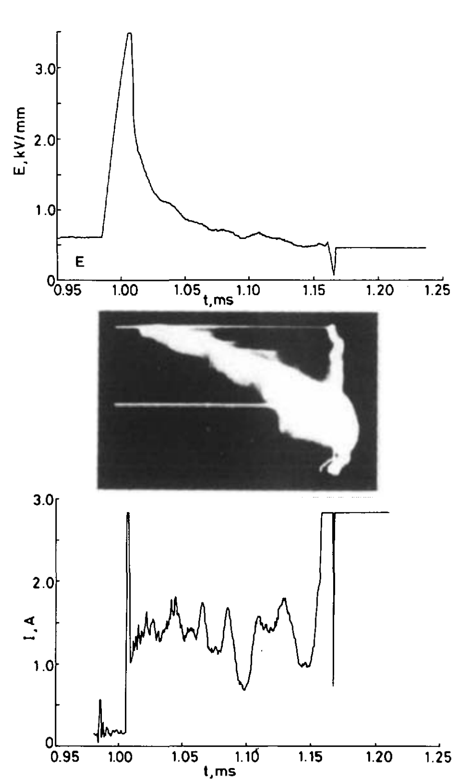

Fig. 18 *Composite record of the positive discharge phase*

The upper oscillogram displays the field probe response, the lower the current. These time displays are synchronized with the image convertor record of the positive discharge.

image-convertor record displays an interesting feature during the later stages of the leader-corona development, which is the rapid axial elongation of this phase. In Fig. 19, information concerning this axial elongation is illustrated with the parameter Δt as variable. For times $\Delta t > 30\,000$ μs the phenomenon is barely discernible, and, in the absence of any pre-existing space charge, does not exist. However the important aspect is that the leader propagation (axial velocity) is virtually unaffected.

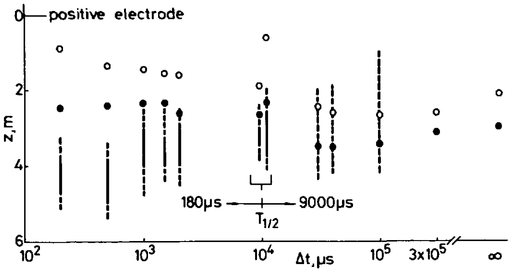

Fig. 19 *Macroscopic characteristics of the positive discharge based on the spatiotemporal streak records*

○ critical leader lengths z_{crit}
● axial positions reached by the leader from which the final jump is launched
The vertical lines indicate the spatial position of the leader corona elongation, and the graded intensity signifies the clarity of these observations. Δt is the time delay to the positive impulse. Critical leader length is identical to a maximum leader length at withstand.

The basic spatial behaviour of the leader is also displayed in Fig. 19 and these data, taken in conjunction with the space-charge field data of Fig. 14, suggest that not only the magnitude but also the time-dependent characteristics of the pre-existing space charge are of major importance in the positive discharge development.

Fig. 18 illustrates typical field and current probe responses in a breakdown situation. It is seen that the recorded field strength rapidly tends to a value similar to that of the pre-existing space-charge field. In the absence of space charge, the recorded field falls essentially to zero, following the leader inception. This suggests that the space-charge field remains as a type of bias field until the breakdown phase (final jump) is precipitated, at which instant the applied voltage collapses. The current oscillogram indicates that a level of $\simeq 1$ A is maintained during leader propagation. The superimposed fluctuations ($\lesssim 0.5$ A) are probably correlated with the slightly discontinuous growth of the leader channel; but, at a later stage, these fluctuations become more vigorous and a time correlation with the axial elongation of the leader corona cannot be excluded.

An interesting feature observed during the positive leader development was the occurrence of leader restrikes (reilluminations), see Fig. 20. These were most pronounced following the 9000 μs impulse, but were virtually absent under the positive impulse alone. Previous observations of this nature with positive impulses were associated with a high ambient humidity (>10 g/m^3) [11]. In the present series of experiments a value of humidity of $\simeq 6$ g/m^3 was always recorded, further confirming the link between the restrikes observed here with the presence of the pre-existing space charge.

At breakdown it is observed that the positive leader may propagate under certain space-charge conditions ($\Delta t > 10\,000$ μs) to an axial position exceeding that reached by the leader when the gap is free from space charge. The corresponding timelags to breakdown are also increased, see Table 1, and reflect the longer duration of the constant-velocity phase of the leader growth. For $\Delta t < 10\,000$ μs, the space-charge fields lead to short breakdown times with corresponding short leader lengths. In Fig. 19 the average axial extents reached by the leaders at the instant of the final jump are indicated; i.e. the time at which the gap between the leader tip and the negative electrode is initially bridged. It is clearly seen that, in the cases of short-tailed impulses, the leader lengths are systematically shorter than those of both the long-tailed wave and for the case of the positive impulse alone.

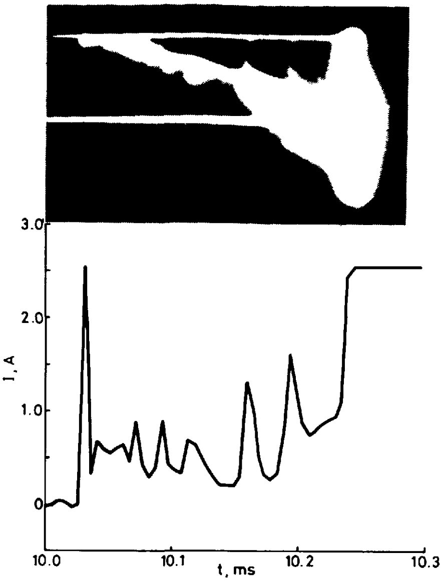

Fig. 20 *Image convertor record of a positive discharge which shows leader restrikes*

$T_{1/2} = 9000$ μs. The associated current oscillogram clearly indicates this phenomenon at time 10.1 ms $< t <$ 10.2 ms; $\Delta t = 10$ ms

For $t < 2000$ μs there is evidence that the negative leader, which can be reactivated several times during the decay of the short tail ($t < 500$ μs), is again reilluminated (see Fig. 21) during the positive leader phase. Hence, there protrudes into the gap an ionised channel which abruptly shortens the gap itself. The average length of this negative leader channel is ~ 1 m, and is directly comparable to the difference in positive leader lengths mentioned previously. At 10 000 μs, there is no indication of any reillumination of the pre-existing negative leader channel and the situation approaches that of the positive impulse alone ($\Delta t = \infty$), see Fig. 19.

The long-tailed impulse exhibits quite clearly, for times in the range $30\,000 < t/\mu s < 100\,000$, a much shorter final

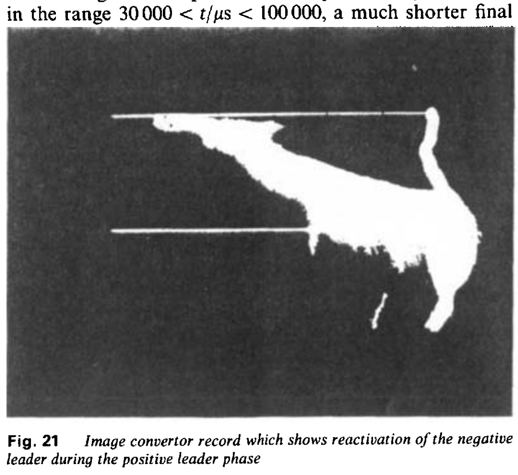

Fig. 21 *Image convertor record which shows reactivation of the negative leader during the positive leader phase*

The positive discharge spans the gap. $\Delta t = 500$ μs.

jump as leader propagation is sustained over very long distances. It is worth noting that the associated positive voltage levels are of the order of those pertaining to a 6 m rod-plane gap under critical waveshape conditions. Owing to such low-voltage levels, it is probable that the conditions for streamers (leader corona) to bridge the gap are fulfilled only at a later stage of the leader propagation. The resultant final jump is, therefore, reduced in length. As Δt is increased, the situation again approaches that of the positive impulse alone and probably reflects the dissipation of the space-charge cloud.

The rôle of the space charge seems to be that of providing, via its associated field, a substantial augmentation of the electrostatic field, particularly in the central region of the gap. The discharge can, therefore, propagate in a region where the geometric field alone would be insufficient. In addition, the negative ions of the space charge could supply initiatory electrons by detachment, and thus facilitate avalanche formation ahead of the leader tip. The smooth propagation of the leader seems to be indicative of a situation in which equilibrium conditions are attained.

The one observation which apparently falls outside the general trend corresponds to a situation ($\Delta t \sim T_{1/2} = 9000$ μs) in which a considerable negative voltage is still applied to the gap at breakdown. The enhanced field in front of the negative electrode might possibly enable a corona discharge from this electrode to reach the approaching positive streamers. A relatively long final jump is then to be expected.

6 Discussion and conclusions

6.1 Pre-existing space charge

A negative impulse ($T_{cr} = 45$ μs) is used to produce a pre-existing space charge in the rod-rod gap, and the magnitude of the space charge recorded at $t = T_{cr}$ is observed to be an increasing function of the impulse voltage amplitude (U_-). This initial space charge is thereafter strongly influenced by the impulse wavetail, i.e. by the rate of decay of the negative voltage. For example, with a 180 μs wavetail, the magnitude of the space charge at T_{cr} is reduced by more than 50% within $\simeq 500$ μs. During this time interval reverse discharges are observed in the vicinity of the negative electrode. Comparable observations have been made with LI voltages (2/45 μs) [9], and qualitatively explained in terms of a field reversal in the cathodic region. For the 9000 μs wavetail, ionic drift controlled by the geometric field produces, at $t > T_{cr}$, a slow increase in the measured charge up to a maximum value at $t \sim 5000$ μs. Thereafter the measured charge slowly decays, but, as reverse discharges are absent, the value remains relatively high at $t = \Delta t$. Consequently, for long Δt values, mutual repulsion of the space charge is considered to be operative [12].

In the present study, attempts to model the space-charge cloud and quantitatively clarify the observed phenomena were undertaken. A basic difficulty lies in the interpretation of the measured charge records. However, when viewed from the positive electrode the pre-existing space charge is seen as a net negative charge. Simple point-charge systems could then be used to successfully generate the space-charge field values recorded at this boundary by the static probe. It should be emphasised that these sytems do not model the true composition of the pre-existing space charge, which recent studies in shorter gaps have shown to be bipolar [13].

6.2 Reduction of insulation strength by pre-existing space charge

To study the interaction of this space charge with the development of the positive discharge, a variable time delay Δt was established between impulses, such that the negative impulse always preceded the positive. It was found that the gap insulation behaviour (U_{50+}) was strongly influenced by the space charge created during the negative impulse application. $U_{50+}(\Delta t)$ was observed to be an inverse function of the space-charge field $E_{sc}(\Delta t)$, and, throughout the range $200 \leqslant \Delta t/\mu s \leqslant 300000$, the measured values were lower than the U_{50+} value obtained with the space-charge-free gap.

For a U_- level of $\simeq 80\%$ of U_{50-}, reductions in the U_{50+} of 60% could be achieved following the 45/9000 μs negative impulse. For the 45/180 μs impulse, reductions of 35% were observed. It should be noted, however, that owing to the Δt-values used these pronounced reductions may, in part, be attributed to the negative voltage component present at the time of breakdown, e.g. $u_{2-} \sim U_{50+}$ for $T_{1/2} = 9000$ μs and $\Delta t = 10000$ μs, whereas $u_{2-} \sim 0.2U_{50+}$ with $T_{1/2} = 180$ μs and $\Delta t = 200$ μs. For increasing values of Δt the withstand level of the gap progressively recovers. Following the creation of the space charge, a time delay of $\simeq 100T_{1/2}$ appears to be sufficient to restore the gap to an effective space-charge-free condition.

For synchronous voltage application ($\Delta t = 0$), the total breakdown voltage ($U_{50+} - u_{2-}$) is, as a first approximation, found to increase linearly with the negative voltage component u_{2-}, while the associated positive component U_{50+} decreases. For nonsynchronous impulses, the total breakdown voltage is less than that of the zero-space-charge condition, $U_{50+}(\infty)$.

6.3 Modification of positive discharge

The positive corona and leader inception levels are clearly reduced by the pre-existing negative space charge. The associated space-charge field assists the leader development both at inception and during propagation. In addition, within the boundaries of its creation, the pre-existing space charge presents a weakened dielectric region to the impinging positive discharge. The interaction of the leader corona with the pre-existing space charge is clearly observed for $\Delta t \leqslant 10000$ μs, as the space-charge region is made manifest by the sudden elongation of the leader corona. For $T_{1/2} = 180$ μs, the clarity of this elongation gradually diminishes with increasing Δt, and probably reflects the decreasing magnitude of the associated space charge. Under such conditions the length of the final jump (as measured from the positive leader) is $\simeq 3.5$ m. However, for the shortest Δt values (<2000 μs), a negative leader of ~ 1 m in total length is observed to develop from the negative electrode during the positive discharge phase. This negative leader retraces the path of the initial negative event.

6.4 Recovery of insulation strength

For $10000 < \Delta t/\mu s \leqslant 100000$, the time dependence of the pre-existing space charge can be observed. Two main features may be identified. The elongation of the leader corona is hardly discernible, if at all present, and the initial space-charge field (1.0 kV/mm at $t = 10000$ μs) decreases to $\simeq 50\%$ of its value within 100000 μs. Although this latter field value is approximately equal to that obtained with the short-tailed impulse, the final-jump length has now decreased by 30% to 2.5 m. The difference in final-jump lengths is probably accounted for by the absence of a negative leader at these longer times. Positive U_{50} values, however, are observed to remain similar in magnitude to those for $\Delta t < 10\,000\ \mu s$.

For $\Delta t > 100\,000\ \mu s$, the final-jump length gradually increases towards the value associated with the zero-space-charge condition ($\Delta t = \infty$). This recovery behaviour presumably reflects the gradual dissipation of the pre-existing space charge. It should be noted that, at these longer Δt values, the reduced influence of the pre-existing space charge is compensated by an increase in the U_{50+} levels.

7 References

1 CIGRÉ TASK FORCE 33.03.03: 'Switching impulse test procedures for phase-to-phase air insulation', *Electra*, 1973, (30), pp. 55–69
2 CIGRÉ WORKING GROUP 33.03: 'Switching impulse strength of phase-to-phase insulation', *ibid.*, 1979, (64), pp. 158–181
3 CIGRÉ TASK FORCE 33.03.03: 'The influence of non standard conditions on the switching impulse strength of phase-to-phase insulation', *ibid.*, 1979, (64), pp. 211–230
4 BALDO, G., PESAVENTO, G., HUTZLER, B., RIU, J.P., FISCHER, A., and ZACKE, P.: 'Phase to phase insulation: space charge effect on discharge development'. *3rd Int. Symp. HV Eng.* (Associazione Elettrotechnica ed Elettronica Italiana, Milan, 1979), Vol. 2, Paper 51.12
5 BISHOP, M.J., and SIMON, M.F.: 'The impulse generators at Les Renardières', *IEEE Trans.*, 1972, **PAS-91**, pp. 2366–2376
6 SINGER, H., STEINBIGLER, H., and WEISS, P.: 'A charge simulation method for the calculation of high voltage fields', *ibid.*, 1974, **PAS-101**, pp. 1660–1668
7 BALDO, G., PESAVENTO, G., HUTZLER, B., RIU, J.P., FISCHER, A., and ZACKE, P.: 'Phase to phase insulation: effect of the shift between the two components of the applied voltage'. *3rd Int. Symp. HV Eng.* (Associazione Elettrotecnica ed Elettronica Italiana, Milan, 1979), Vol. 2, Paper 52.18
8 LES RENARDIÈRES GROUP: 'Negative discharges in long air gaps at Les Renardières — 1978 results', *Electra*, 1981, (74), pp. 67–216
9 KLEIMAIER, M., HUTZLER, B., and BÖCKER, H.: 'Space charge effects in negative rod-plane discharges'. *IEE Conf. Publ. 189*, 1980, Part 2, pp. 191–194
10 ZACKE, P.: 'Durchschlag der Stab-Stab-Anordning in atmosphärischer Luft bei kombinierter Beanspruchung mit zwei Stoßspannungen entgegengesetzter Polarität'. Dissertation, University of Stuttgart, 1979
11 LES RENARDIÈRES GROUP: 'Positive discharges in long air gaps at Les Renardières — 1975 results and conclusions', *Electra*, 1977, (53), pp. 31–153
12 McDANIEL, E.W.: 'Collision phenomena in ionized gases' (Wiley, New York, 1964), pp. 518–521
13 ALLEN, N.L., CLARK, P., DRING, D., and WATERS, R.T.: 'Ionic combination and the estimation of the negative ion component in positive corona'. *8th Int. Conf. Gas Discharges & Appl.*, Oxford, 1985 (University of Leeds Press), pp. 163–166
14 SCHUMANN, W.O.: 'Über das Minimum der Durchbruchfeldstärke bei Kugelelektroden', *Arch. Elektrotech.*, 1923, **12**, pp. 593–608
15 VON ENGEL, A.: 'Ionized gases' (Oxford University Press, London, 1965, 2nd edn.), pp. 112–138
16 RAETHER, H.: 'Electron avalanches and breakdown in gases' (Butterworths, London, 1964), pp. 56–90

8 Appendixes

8.1 *Influence of the pre-existing space charge on the corona onset field strength of the positive electrode*

I.W. McALLISTER and G.C. CRICHTON

8.1.1 Introduction: As indicated in Section 5.2, the pre-existing negative space charge continues to exist in the gap for times $t \geqslant \Delta t$, such that, at these times, a finite value of field strength is present at the positive electrode boundary. This field strength E_{sc} supplements the geometric field E_g of the positive impulse which is applied at $t = \Delta t$. In the present contribution, the influence of E_{sc} on the value of E_g required to produce corona onset at the positive electrode is investigated analytically. The onset field strength is the minimum value of electric field strength at the electrode surface which can initiate a corona discharge.

For $\Delta t/T_{1/2} < 3.5$, the value of the negative impulse $u_-(\Delta t)$ is finite (see Table 1), and, hence, at $t \leqslant 3.5T_{1/2}$, there is, in addition to E_{sc}, a measurable geometric field component. This geometric field will augment that produced by the subsequent positive impulse. With respect to corona onset calculations, interest is centred on the variation of the resultant electric field distribution in the vicinity of the positive electrode, i.e. for $0 \leqslant z/R \leqslant 0.5$, see Fig. 22. As in this region the geometric electric field distribution is effectively controlled by the geometry of the electrode alone, we can consider the geometric fields produced

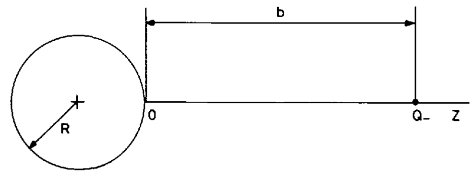

Fig. 22 *Modelling of the space-charge field E_{sc} with reference to the positive electrode*

by $u_-(t)$ and $u_+(t - \Delta t)$ to be produced by an equivalent positive voltage.

8.1.2 Modelling E_{sc}: Fig. 19 indicates that, for $\Delta t < 300\,000\ \mu s$, the space charge remains at least 2 m distant from the positive electrode. Thus, with respect to this electrode, the space charge may, as a first approximation, be represented by an equivalent negative point charge Q_-. In addition, as the spherical termination of the positive electrode is of radius 0.125 m, this electrode may with respect to corona onset calculations be modelled as an isolated sphere. Hence, using the method of images, the axial space-charge field may be expressed as (see Fig. 22)

$$E_{sc}(z) = \frac{Q_-}{4\pi\varepsilon_0 R^2}\left[\frac{1}{(b/R - z/R)^2} + \frac{1 + b/R}{(b/R + (1 + b/R)z/R)^2}\right] \tag{4}$$

From this expression, it is clear that a selected $E_{sc}(0)$ value may be obtained with various combinations of Q_- and b. By this means, the effect of the space-charge field distribution $E_{sc}(z)/E_{sc}(0)$ on the onset field strength can be examined. For the range of Δt used in these studies, Fig. 14 indicates that the recorded values of $E_{sc}(\Delta t)$ did not exceed ~ 1 kV/mm. A similar upper limit will be imposed on $E_{sc}(0)$.

8.1.3 Corona onset calculations: To illustrate the influence of E_{sc} on corona onset, a comparison of the geometric onset field strength with, E_{osc}, and without, E_0, the pre-existing space charge is undertaken. The calculations were performed using the classical Schumann approach [14] with the limiting field strength for ambient air being taken as 2.42 kV (mm bar)$^{-1}$. Atmospheric pressure is assumed to be 1 bar (0.1 MPa). Under these conditions, we find that, for a Laplacian field, the corona onset field strength E_0 is 3.27 kV/mm for $R = 125$ mm. The results of the calculations are given in Fig. 23 for $b/R = 20$. As the variation in the space-charge field distribution $E_{sc}(z)/E_{sc}(0)$ for the appropriate range of Q_- and b values is, on examination, found to be negligible, E_{osc} becomes independent of this factor.

A regression analysis of associated values of E_{osc} and $E_{sc}(0)$ indicated that these two parameters are, in the

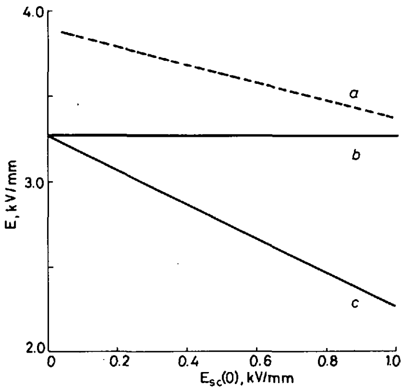

Fig. 23 *Variation of corona field strength with the space charge field $E_{sc}(0)$ for $b/R = 20$*

a Total corona inception field strength; experimental (see Fig. 16, curve *a*)
b Total corona onset field strength ($E_{osc} + E_{sc}(0)$)
c Geometric corona onset field strength E_{osc}

present conditions, linearly related, see Fig. 23*c*. This relationship can be expressed as

$$E_{osc} = E_0 - E_{sc}(0) \tag{5}$$

implying that the total corona onset field strength is constant, namely E_0, see Fig. 23*b*.

8.1.4 Discussion and conclusion: For a Laplacian field, the present calculations indicate that the normalised critical avalanche length z_0/R has a value of 0.162. This distance parameter is defined by

$$E_t(z_0/R) = 2.42 \text{ kV/mm} \tag{6}$$

An examination of the space-charge field distribution $E_{sc}(z)/E_{sc}(0)$ and the geometric field distribution $E_g(z)/E_g(0)$ in the range $0 \leqslant z/R \leqslant z_0/R$ reveals that these distributions are effectively identical. This implies that the field distributions associated with the total field E_t is the same as the original Laplacian distribution, i.e.

$$\frac{E_{sc}(z)}{E_{sc}(0)} = \frac{E_g(z)}{E_g(0)} = \frac{E_t(z)}{E_t(0)} \tag{7}$$

Hence, as the magnitude of the corona onset field strength, equivalent to the appropriate value of either $E_t(0)$ or in the absence of space charge $E_g(0)$ ($\equiv E_0$), is controlled by the field distribution, then

$$E_{0t} \equiv E_0 \tag{8}$$

with E_{0t} being the total onset field strength. In addition, under space-charge conditions we have

$$E_t(0) = E_g(0) + E_{sc}(0) \tag{9}$$

and, hence, eqn. 5 follows automatically, as at corona onset $E_g(0)$ is identical to E_{osc}.

With the use of impulse voltages, the initial corona discharge does not occur at the minimum possible field strength, the onset level E_0, owing to the lack of an initiatory electron. The time lag to the availability of this electron implies that the corona discharge must occur at an increased field strength, namely the inception level E_i. The longer this statistical time lag t_s, the greater becomes the difference ($E_i - E_0$). One method of reducing t_s is to apply an appropriate sweep field. In this study, the space-charge field can act in this manner, and, consequently, the greater the established E_{sc}, the smaller t_s will become such that $E_i \rightarrow E_0$. This behaviour pattern is illustrated by curves *a* and *b* in Fig. 23 for increasing values of E_{sc}. Fig. 23*a* relates to the (average) total inception field strength E_{it} recorded experimentally, see Section 5.3.

In conclusion, as the initial corona develops in immediate proximity to the electrode, a linear relationship is found to exist between the geometric onset field strength and the magnitude of the space-charge field at the electrode. In addition, the space charge field is seen to act as a sweeping field with respect to the initiatory electron, such that the total inception field strength tends towards the total onset field strength for increasing values of the space-charge field.

8.2 On the rapid elongation of the leader corona

R. Diaz, B. Hutzler and G. Riquel

8.2.1 Introduction: When the positive impulse, which is applied to the sphere, is triggered less than 30 ms after the space-charge injection, a rapid elongation of the leader corona ('elongation' in the following) is observed. This is illustrated by Figs. 18 and 19. This appendix deals with the causes and consequences of this unusual phenomenon which does not exist without pre-existing space charges.

8.2.2 Additional experimental results: The case which is selected for the detailed analysis of the phenomenon corresponds to the negative impulse of $U_- = -2250$ kV with a long tail (9000 μs) and a positive impulse delay of 10 ms. In such conditions, it has been shown in Part 4 that the maximum measured charge q_- can be regarded as the true net charge injected into the gap. Furthermore (Fig. 5*a*), this injected charge q_- is largely variable and is correlated to the total length Z_- of the negative discharge. Fig. 2 shows data obtained during an up and down procedure, so that the amplitude U_+ of the positive impulse varies from 665 kV up to 1082 kV.

The elongation of the leader corona is characterised by its instantaneous inception voltage u_{+r}, the length reached by the positive leader Z_{+r} when it occurs, and by the overall length of the positive discharge just before (S_{0r}) and just after (S_r) the elongation. All these data are given as a function of q_- in Fig. 24, which shows that the higher the injected charge q_-, the lower the instantaneous voltage u_{+r}, independent of the crest voltage of the positive impulse.

8.2.3 Field analysis: The visual appearance of the phenomenon suggests that it is related to the existence of a minimum of the electric field, which has to be overcome for the discharge to continue its propagation. The electric field which causes the positive discharge to propagate is the combination of the field created by the positive leader itself and of a 'guiding field' which is composed of a geometrical field (due to the voltages applied to both electrodes) and of the field created by the pre-existing space charge. Let us analyse, simply and qualitatively, how this guiding field changes with time.

As shown by a number of consequences, the pre-existing space charge can be simulated by a negative charge located at the tip of the negative discharge. As a function of time, this charge is subjected to drift and self-expansion. On the basis of the simple model of spheric expansion, the spheric cloud reaches a radius R after a time T given by

$$R^3 = R_0^3 + \frac{3\mu QT}{4\pi\varepsilon_0} \quad (10)$$

With $\mu = 1.4\ 10^{-4}\ \mathrm{m^2/V.s}$ and $Q = 75\ \mu C$ we get $R = 1.4$ m after $T = 10$ ms if we neglect R_0^3 with respect to R^3.

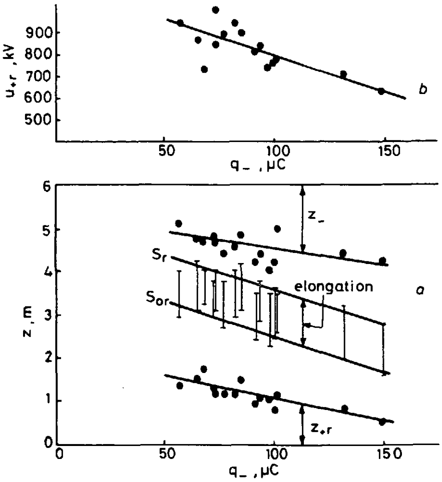

Fig. 24 *Experimental results for the up and down test*
$T_{1/2} = 9$ ms, $\Delta t = 10$ ms, $U_- = -1040$ kV
a Geometrical parameters: Z_- = length of the negative discharge, Z_{+r} = positive leader length at the 'elongation' inception, S_{or} = overall positive discharge length at the 'elongation' inception, S_r = overall positive discharge length after the 'elongation'.
b Positive inception voltage for the 'elongation'

During the same time, the drift is limited to a few tens of centimetres, so that the expansion can be considered as the most efficient phenomenon. On this basis, the field at a given location can be regarded as constant, as long as this point remains outside the cloud of space charge.

Fig. 25 gives the potential and field distributions inside the gap without space charge (*a*) and with space charge (*b*, *b'*, ...). Without space charge, the electric field exhibits one minimum which is roughly in the middle of the gap. When the streamers reach this minimum (shifted towards the cathode by the presence of the positive leader channel), they can develop to the cathode. This is what happens at the beginning of the final jump.

With space charge, for a long time following the negative charge creation, the field distribution in the gap will be characterised by two minima *m* and *m'* separated by a maximum *M* which follows the charge-cloud boundary. In such a field configuration, assuming that the effect of the positive leader channel remains constant, when the streamers of the leader corona reach the minimum *m* they will be able to continue their propagation toward the second field minimum *m'* which is near the cathode.

8.2.4 Discussion: With passage of time, the field maximum *M* (the boundary of the charge cloud) reaches position *m*. At that time, the field distribution returns to the usual shape with only one minimum, and the elongation is no longer observed. Experimentally, this occurs for $\Delta t \geqslant 40$ ms. Eqn. 10 shows that an average charge of 75 μC reaches a radius of 2.25 m after 40 ms. This order of magnitude is satisfactory, as it can be seen in Fig. 24*a* that between the tip of the negative discharge and the overall length of the positive discharge just before the elongation (S_{or}) is a distance of about 1.85 m is measured.

Quantitative evaluation of the guiding field distribution shows that the position of the field minimum is closer to the anode when the negative discharge becomes stronger.

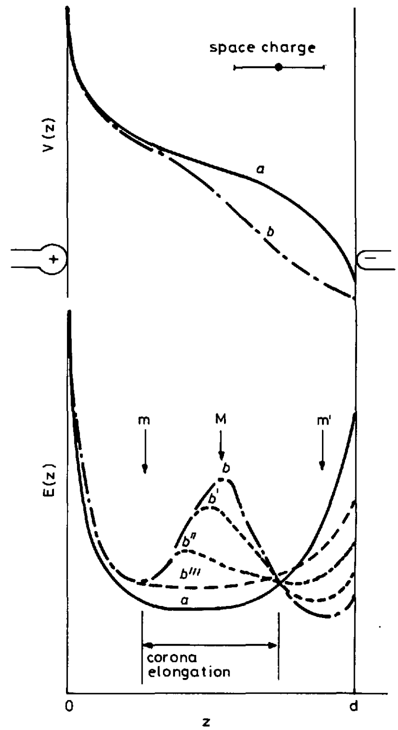

Fig. 25 *Sketch of potential and field distribution*
(*a*) Without pre-existing space charges
(*b b' b'' b'''*) With space charges at different stages of the charge expansion

This position is compared with Z_{+r}, S_{or} and S_r in Fig. 26. An entirely quantitative comparison between *m* and S_{or} is not conclusive due to the important influence of the positive leader channel on the field. However, this result supports the previous interpretation of the elongation.

It has already mentioned that the elongation is comparable to a final jump. In fact, if the elongation does not appear, breakdown never occurs and, when the elongation occurs, breakdown always follows. Fig. 26, for instance, compares the positive leader tip position when the elongation occurs in case of breakdown, with the maximum length reached by the positive leader in case of withstand.

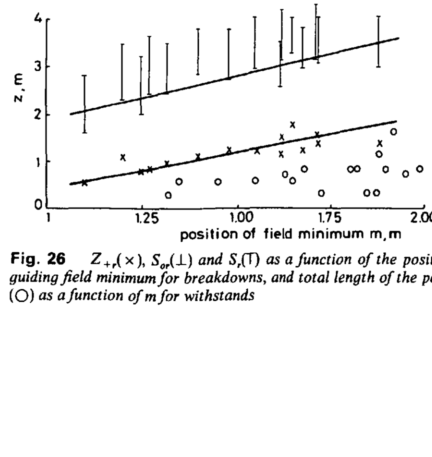

Fig. 26 $Z_{+r}(\times)$, $S_{or}(\perp)$ *and* $S_r(\top)$ *as a function of the position m of the guiding field minimum for breakdowns, and total length of the positive leader* (O) *as a function of m for withstands*

It can be seen that, in all cases of withstand, the leader tip remains blocked behind the field minimum. This suggests that, for breakdown, as for the elongation inception, U_+ and q_- have to combine in appropriate proportion. Fig. 27 shows the results, i.e. breakdown or withstand, collected during the up and down test procedure for all shots characterised by U_+ and q_-.

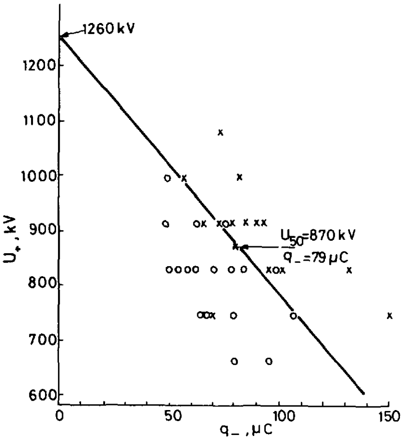

Fig. 27 *Representation of the up and down test characterising the shots by the positive crest voltage U_+ and the pre-existing negative space charge q_-*

—— $U_+ + q_-/C = 1260$ with $C = 215$ pF
O withstands
× breakdowns

It can be seen that an equivalent breakdown voltage can be defined:

$$U_{eq} = U_+ + q_-/C = 1260 \text{ kV} \quad C = 215 \text{ pF} \tag{11}$$

From this graph, it becomes obvious that the standard deviation attached to the up and down procedure is, for a large part, imposed by the dispersion of the negative pre-existing charge which acts as an uncontrolled parameter.

An important result must be underlined. The $U_+ - q_-$ graph of Fig. 27 exhibits a clear separation between breakdowns and withstands. This is also true for $\Delta t = 30$ ms, but, for longer values of Δt, this separation tends to disappear and no distinction can be made between the population of breakdowns and withstands. This must be related to the fact that the elongation disappears for $\Delta t > 30$ ms and confirms the correlation between the elongation and breakdown.

For $\Delta t \geqslant 40$ ms the elongation is absent and the breakdown probability is no longer linked to the negative space charge injected into the gap. However, the U_{50} breakdown voltage still remains lower than the value without space charge. On the basis of Fig. 25, this appears to be due to a redistribution of the field in the gap. The space charge increases the field in the anodic region and decreases it in the cathodic region, making the field distribution closer to the distribution in a rod-plane gap.

Quantitatively, the border line of Fig. 27 passes through the average point ($U_{50} = 870$ kV, $q_- = 79$ μC) and crosses the U_+ axis for $U_+ = 1260$ kV. This is the positive voltage which would have to be applied to the gap to reach a breakdown without pre-existing space charges. As a matter of fact, taking into account that the negative instantaneous voltage is -1040 kV, it can be seen that this pair ($U_+ = 1260$ kV; $U_- = -1040$ kV) is nearly on curve *a* of Figure 2. Owing to the small number of results, it would be too bold to generalise this result, but this equivalence between negative charge and positive voltage could be a starting point for future work.

8.3 The influence of the pre-existing space charge on the critical length of the positive leader

G.C. Crichton and S. Vibholm

8.3.1 Introduction: From the point of view of engineering design, the discharge conditions associated with the minimum breakdown voltage are of major interest. Of direct importance are the macroscopic parameters U_{50+} and the time lag to breakdown T_B. As leader growth is observed to be the longest single event in both spatial extent and time, this latter parameter directly reflects the leader stage of the breakdown process. A knowledge of the minimum positive leader length, which can ultimately lead to breakdown, is therefore of interest. In the present experimental study, the interaction of the leader phase with a pre-existing net negative space charge is seen to be considerable. In this appendix, an attempt to illustrate this interaction in a quantitative manner is undertaken.

8.3.2 Critical leader criterion: A minimum or critical leader length z_{crit} is associated with a time T_{crit}, which represents the instant when the electrostatic field conditions first become such that breakdown is inevitable. The necessary condition is defined empirically to be attained if $E_L(z)$, the average gradient in the advancing positive leader of axial length z, falls below the instantaneous field value determined by the average gradient in the unbridged gap (see Reference 11, in particular pp. 89–97). To include the presence of a space-charge field, this criterion may be formulated as follows:

$$E_L(z) \pm E_{sc}(z) < \frac{u_+(t) - zE_L(z)}{d - z} \tag{12}$$

where d is the gap length and $u_+(t)$ the instantaneous value of the applied positive voltage. The parameter z is the axial distance from the positive electrode boundary. $E_{sc}(z)$ is the average space-charge field along the path of the advancing positive leader. For a net negative space charge this quantity decreases the left-hand side of the inequality, resulting in a smaller value of z_{crit}. This value of z is the axial length of the leader for which the inequality is first satisfied. Hence, from eqn. 12 it is possible to infer that the presence of a negative-space-charge field should lead to an effective leader-to-breakdown propagation at smaller z_{crit} values than observed in a space-charge-free gap. In addition, if leader velocities for various space-charge environments remain essentially equal, then, on the basis of eqn. 12, the larger negative-space-charge fields should be associated with lower positive applied voltages at breakdown.

8.3.3 Application of the criterion: In the present experimental study, this breakdown pattern is basically observed for times up to $\Delta t \leqslant 10\,000$ μs ($T_{1/2} = 180$ μs), and Fig. 28 shows the agreement achieved between experimental and calculated values of z_{crit} based on the above. The inequality is used to establish the limits of z_{crit}: the upper limit is computed using values of E_{sc} measured at the positive electrode boundary (Section 5.2), whereas the lower limit represents a space-charge-free condition. Numerical values of the function $E_L(z)$ are computed using the data available from previous long-gap studies (Reference 11, in particular pp. 77–85). For the 180 μs wavetail and $\Delta t \leqslant 10\,000$ μs, the upper limit is seen to represent quite accurately the experimental observations.

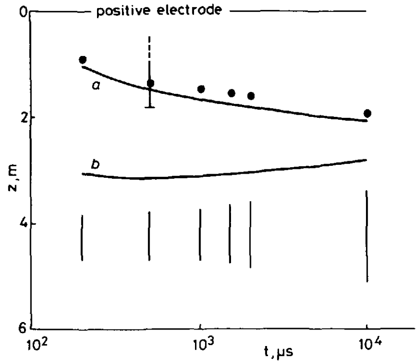

Fig. 28 *Comparison of the computed and experimental values of* $z_{crit} - T_{1/2} = 180\ \mu s$
● experimental
a Upper limit, computed
b Lower limit, computed
The vertical lines illustrate the expansion of the space-charge cloud boundary with time

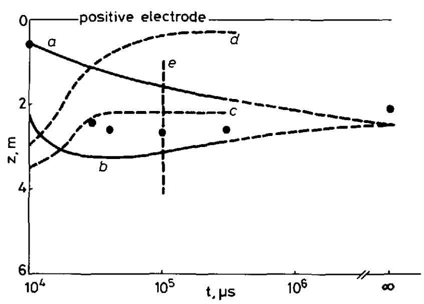

Fig. 29 *Comparison of the computed and experimental values of* $z_{crit} - T_{1/2} = 9000\ \mu s$
● experimental
a Upper limit, computed
b Lower limit, computed
The value at $t = \infty$ is computed for the space charge free condition.
c and *d* Computed space-charge cloud centre and periphery, respectively
e Corona elongation at $\Delta t = 100\,000\ \mu s$ (experimental)

An extension of this procedure to times $\Delta t \geqslant 10\,000\ \mu s$ ($T_{1/2} = 9000\ \mu s$) is illustrated in Fig. 29. The anomalous behaviour of z_{crit} for $30\,000\ \mu s < \Delta t < 100\,000\ \mu s$ is most evident with the experimental values approaching the lower computed limit. The occurrence of these long z_{crit} values is considered to be associated with the displacement and expansion of the space-charge cloud which is probable, due to the much longer time intervals involved. Displacement of the space-charge cloud centre will be towards the positive electrode with the periphery of the cloud continuously expanding due to mutual repulsion [12].

A reduced leader conductivity might possibly account for these observations, but, because the average current levels are basically unaltered (see Table 2, Section 5), the emphasis should be on the evolution of the pre-existing space-charge cloud.

8.3.4 Mutual repulsion of the space charge: It is readily shown for a spherical charge distribution of radius r that

$$\frac{dr}{dt} = \mu Q/(4\pi\varepsilon_0 r^2) \tag{13}$$

where Q is the magnitude of the space charge and μ is the ion mobility. If eqn. 13 is solved for r and expressed as a function of time, we may examine the expansion of the space-charge cloud with time.

Let us assume that at time t ($\Delta t = 10\,000\ \mu s$) the initial conditions are $E_{sc}(z = 0) = E_{sc}(\Delta t)$, see Fig. 14, Section 5.2, and that the space-charge centre is located on the gap axis at a distance $z = 3.5$ m from the positive electrode, see Fig. 19, Section 5.4. The magnitude of the space charge is computed as

$$Q \simeq E_{sc}(\Delta t) 4\pi\varepsilon_0 R z^3/(R^2 - D^2) \tag{14}$$

where R is the radius of the positive electrode and D is the radial distance to the location of the effective point charge Q. The initial radius r_0 of the space-charge cloud is governed by the condition $E(r_0) < 2.42$ kV/mm. The expansion of this cloud with time is then examined in conjunction with a superimposed drift owing to the negative voltage component remaining up to a time of $32\,000\ \mu s$. The value of Q is continuously modified to reflect the experimentally observed $E_{sc}(\Delta t)$ function. Values for mobility μ are placed in the range $10^{-4}\ m^2/Vs < \mu < 2 \times 10^{-4}\ m^2/Vs$ [15], and, owing to the midgap location of the space-charge centre, a drift velocity of ~ 75 m/s is considered appropriate [16]. The results of this computation are presented in Fig. 29.

8.3.5 Discussion and conclusion: It is seen that, in the range $t \geqslant 30\,000\ \mu s$, the boundary of the space-charge cloud can expand to intercept the advancing leader in a region corresponding to the computed upper limit of the critical leader length. The value of $E_{sc}(z)$ to be inserted in the inequality may thus be reduced as z now lies within the space-charge boundary. A reduction in E_{sc} requires that z must increase to satisfy the critical condition of eqn. 12. Consequently, the leader advances into the gap.

A further aspect is that the space-charge centre is seen to progress to a point closer to the positive electrode than z_{crit} for the space-charge-free condition. Thus, the propagating leader must enter a region of the gap in which the space-charge field is reversed in direction. The associated reduction in $E_{sc}(z)$ could then account for the propagation of the leader to points in the gap beyond the value of z_{crit} for the space-charge-free situation. In addition, it is observed that, for $t > 30\,000\ \mu s$, the net space-charge density ρ would be reduced to $< 0.1\ \rho_0$, where ρ_0 is the space-charge density at $t = 10\,000\ \mu s$. This pronounced reduction in charge density probably accounts for the diffuse nature of the leader-corona elongation at long Δt values, see Fig. 19, Section 5.4.

For $\Delta t \leqslant 10\,000\ \mu s$, the short critical leader lengths and distinct corona elongations are thus to be expected, because both axial drift and radial diffusion of the space-charge clouds will be much less pronounced. Development of the space-charge boundary for $T_{1/2} = 180\ \mu s$, based on the measured $E_{sc}(\Delta t)$ values, is shown in Fig. 28. These spatial locations should be compared with the corona elongation pattern illustrated in Fig. 19, Section 5.4.

Fig. 29 indicates that space-charge-free conditions are effectively reached for $t \gtrsim 100\,000\ \mu s$, at which time ρ is $\lesssim 0.02\ \rho_0$. The density ρ at these times is of the order $10^{-7}\ Cm^{-3}$. Similar charge density is computed for the $180\ \mu s$ wavetail at a time $\gtrsim 10\,000\ \mu s$. Hence, space-charge-free conditions should be established in general for $\Delta t \gtrsim 100 T_{1/2}$, as is observed experimentally.